

RESEARCH ARTICLE

10.1029/2017JC013501

Key Points:

- A 3-D realistic model is used to examine the Green Island wake mechanism and compensates for the inadequacy of observations
- Green Island wakes are similar to classical von Kármán vortex streets, but are modified by inertial and barotropic instability
- The island-shelf and the tilted lateral shear induce strong vertical shear along the front between the Kuroshio and the wake

Supporting Information:

- Figure S1

Correspondence to:

M.-H. Chang,
minghueichang@ntu.edu.tw

Citation:

Liu, C.-L., & Chang, M.-H. (2018). Numerical studies of submesoscale island wakes in the Kuroshio. *Journal of Geophysical Research: Oceans*, 123. <https://doi.org/10.1029/2017JC013501>

Received 15 OCT 2017

Accepted 4 MAY 2018

Accepted article online 12 MAY 2018

Numerical Studies of Submesoscale Island Wakes in the Kuroshio

Chih-Lun Liu¹  and Ming-Huei Chang¹ ¹Institute of Oceanography, National Taiwan University, Taipei, Taiwan

Abstract Submesoscale wake formation at Green Island (~7 km) in the Kuroshio is examined by the three-dimensional numerical simulations, which are validated by field observations. On the basis of geophysical (rotating and stratified) flow, the wake exhibits sequentially detached recirculation, containing upwelling of cold water, propagates downstream via advection, forming an along-stream oscillating wake, resembling to the von Kármán vortex streets (VKVS). Evidence includes (1) the shedding frequency as a function of the horizontal eddy viscosity shows a trend analogous with classical wakes; (2) the wake behaviors depend on the Reynolds number (Re), where the turbulent transition regime is determined; and (3) the aspect ratio of the island wakes is similar to the ratio of the VKVS. Unlike classical wakes, the vortex street features are adapted by inertial and barotropic instabilities. The inertial instability has large growth rate and tends to slightly destabilize the anticyclonic recirculation. The barotropic instability could be a secondary process to generate eddy kinetic energy at downstream. Finally, our model suggests the hotspot of the turbulent mixing in the wake is located at the plane free shear layer as a result of the vertical shear instability, which is induced by the island-shelf effect and the tilting of the vertical vorticity.

1. Introduction

Small island wakes are a submesoscale process for which the Rossby (ζ/f) and Richardson numbers in the wake region are $\sim O(1)$, where ζ is the relative vorticity and f is the planetary vorticity. The processes make a significant contribution to the vertical flux of mass, heat, salt, nutrient, etc. They also change the upper-ocean stratification and mixed-layer structures (Thomas et al., 2008) via upwelling/downwelling and turbulent mixing (Chang et al., 2013; Hasegawa et al., 2004). Studies of satellite images revealed possible upwelling (e.g., Hsu et al., 2017). Mixing processes and the so-called island-mass effect can be seen around islands (Doty & Oguri, 1956). Accordingly, Hasegawa et al. (2004) investigated the increase of biomass and high productivity due to wakes.

The study of island wakes has a long history. There are two types of island wakes in terms of the forcing. First, wind wakes resulting from an island obstacle produce Ekman surface layer transport, driving thermocline displacements. Strong heat storage and consequent high surface sea temperature will occur at the lee of the island (Caldeira et al., 2005) due to the weak wind mixing. Second, to our interest, the current induced wakes result in colder, saltier water, with higher chlorophyll-a concentrations at the lee of the island, and produces isopycnal doming at the lee of the island (e.g., Chang et al., 2013; Hasegawa et al., 2004).

On the basis of a homogeneous fluid in a nonrotating frame (a general setting of water tank experiment), a steady flow passing an obstacle is well characterized by the unperturbed upstream velocity (U), diameter of the obstacle (D), and the horizontal eddy viscosity (ν_H). Therefore, the dimensionless number, Reynolds number ($Re = UD/\nu_H$) is formed. A series of experiments was conducted by changing the Re (Tritton, 1988). When $Re \ll 1$, the flow is symmetric in the upstream and downstream and is well attached to the obstacle, which is defined as a laminar flow. The symmetry disappears when $4 < Re < 40$. A laminar separation occurs and two attached eddies are formed behind the obstacle. When $40 < Re < 1,000$, the formation of VKVS can be seen, and eventually when $Re > 1,000$, the separated flow becomes turbulent. Theoretically, the spatial distribution of the shedding eddies obeys the aspect ratio. The ratio of the distance between two vortices in different rows h to the distance between two vortices in the same row a has a value of 0.281 (von Kármán & Rubach, 1912). Otherwise, Strouhal number ($St = D/TU$) is critical to determine oscillating period in the wake, where T is the shedding period of the eddy. The St versus Re diagram represents the shedding frequency

varies with Re , which has been derived in numerous numerical and laboratory experiments (Coutis & Middleton, 2002; Roshko, 1993; Relf & Simmons, 1924; Williams, 1988). We borrow the Re - St diagrams to verify our present model.

Geophysical wakes exhibit different characteristics (e.g., Caldeira & Sangra, 2012) from the wake in the water tank. In geophysical flow, the horizontal eddy viscosity (ν_H) is 10 orders of magnitude greater than the molecular viscosity. Hence, the eddy viscosity is more commonly used than the molecular viscosity when considering geophysical wakes. However, an inevitable problem is to determine a proper value for ν_H , since the diffusion given in the model is a combination of physical diffusion and numerical diffusion. In the oceanic flow, the range of the horizontal eddy viscosity is $10^2 - 10^5 \text{ m}^2\text{s}^{-1}$ from place to place (Apel, 1987). As far as the model viscosity is concerned, the magnitude is typically $<10^2 \text{ m}^2\text{s}^{-1}$. Other dimensionless numbers such as the Burger number ($Bu = R_d^2 / D^2$), Rossby number ($Ro = U / fD$), and Ekman number ($Ek = \nu_H / fD^2$) are critical to determine wake performance, where R_d is the baroclinic deformation radius ($R_d = NH / f$), where N is the buoyancy frequency, H is the vertical scale, and f is the Coriolis force. In this study, the Rossby radius (~ 20 – 50 km) is larger than the island scale (~ 7 km), that is, the Earth rotation has only a minor effect. The Rossby number versus Ekman number diagram from water tank experiments (Baines & Davies, 1980) is useful to define different wake behaviors. The asymmetric development of cyclonic and anticyclonic recirculation has been studied by numerical modeling (Dong et al., 2007). The normalized vorticity difference between cyclonic and anticyclonic recirculations ($|Vor-| - Vor(+)| / f$) downstream of the island differs from a dimensionless number $\lambda = Ro / Bu$. The asymmetry of the wake rises when the Ro / Bu exceeds ~ 0.2 . Large and small Re values, respectively, lead to the predominance of cyclonic and anticyclonic recirculation. If the cyclonic recirculation is predominant, anticyclonic recirculation tends to be distorted by the inertial instability.

Island wakes can be categorized as shallow-water and deep-water wakes with the consideration of distinct vorticity generation mechanisms (Tomczak, 1988). In shallow-water wake conditions, the effect of the bottom friction becomes important. Disregarding the Coriolis effect (Ro is large), the recirculation is in a perfect cyclostrophic balance between the centrifugal force (CF) and the pressure gradient force (PGF). The centrifugal force is weakened by the bottom friction, whereas the pressure gradient force remains constant at all depths. Thereafter, the PGF has a weak CF to balance at the bottom, thus the bottom water flows radially inward, forming an upwelling at the center and downwelling at the margin (Wolanski & Hamner, 1988). In a deep-water wake scenario, a “tea-cup effect” is no longer applicable. The upwelling is promoted by entrainment from horizontal surface jets behind the island, carrying the waters at the lee of the island downstream. Consequently, to compensate the surface loss of water and divergence at the lee of the island, an upwelling is induced (Hasegawa et al., 2004).

The Kuroshio is a strong western boundary current in the northwestern Pacific Ocean, and flows northward along the east coast of Taiwan with a width of about 100–150 km and with a speed of 1–1.5 m s^{-1} . It passes Green Island, about 50 km off the east coast of Taiwan (Figure 1), providing a natural laboratory for studying the geophysical island wakes in submesoscale and in deep water. Chang et al. (2013) conducted a series of field experiments to investigate the wake characteristics, including their surface patterns and vertical structures. Dimensionless numbers such as the Reynolds number, Rossby number, and Burger number were estimated to preliminarily examine the dynamic regime of Green Island. However, detailed dynamics underlying the submesoscale wake formation and evolution is absent since only two mappings of wake pattern were conducted and the wake patterns lose synopticity. As reported in Chang et al. (2013), the wake flow is strongly dissipative with a turbulent kinetic energy dissipation rate $O(10^{-7} - 10^{-5}) \text{ W kg}^{-1}$.

Using numerical results in the present work, we interpret the wake evolution in the lee of the Green Island and attempt to address some dynamical issues raised in Chang et al. (2013), including (1) Is the Green Island wake a typical von Kármán wake (vortex street pattern)? (2) Does barotropic and/or baroclinic instability play a role in its dynamics? (3) Does the inertial instability occur in the anticyclonic recirculation of Green Island wakes, as described in previous water tank and numerical experiments? (4) What processes cause the enhancement of turbulent mixing? Re - St diagrams derived from previous numerical and laboratory experiments and field observations are used to validate our proposed numerical model. All of the above mentioned questions will be explored and discussed. Some analyses in this paper such as the wake instabilities are motivated by Dong et al. (2007). The remainder of this paper is organized as follows. Section 2 introduces some background and field observations. Section 3 presents the model configuration. Section 4 presents the

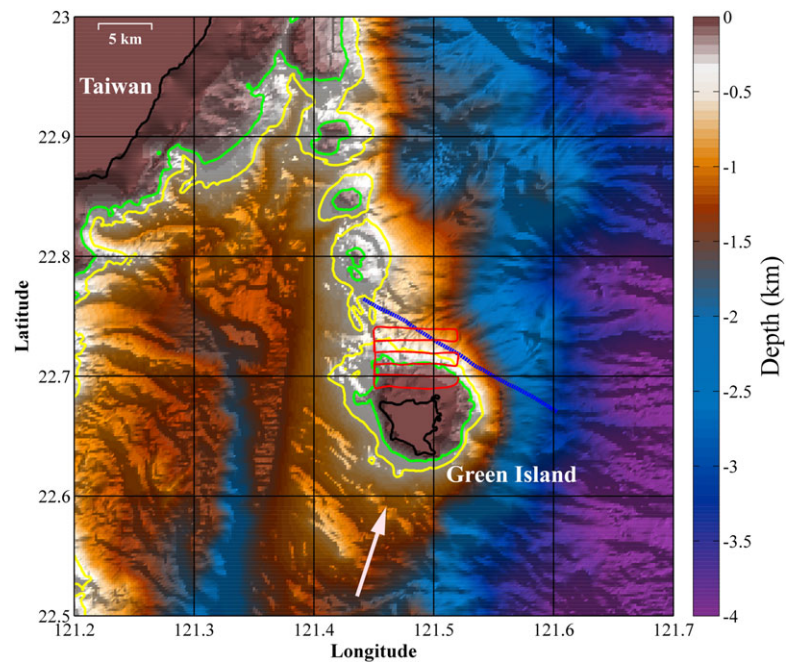


Figure 1. Bathymetry around Green Island; the blue dashed line is the experimental transect of survey 1 (OR3–1712); the red track behind Green Island indicates the ship track of survey 2 (OR3–1780). Depth contours of -250 and -500 m are represented in green and yellow contours, respectively. The white arrow shows a schematic view of the Kuroshio.

results of sensitivity tests and validation of the numerical model. Section 5 discusses wake properties and dynamics. Section 6 presents conclusions.

2. Background and Data

The Kuroshio current flows northeastwardly along Taiwan's east coast with a width of 100–150 km and a maximum speed of $1\text{--}1.5\text{ m s}^{-1}$. The bathymetry southeast of Taiwan is shown in Figure 1. The dominant topographic feature is Green Island, located at the south of the submarine ridges which extend from Green Island to Taiwan's east coast. Green Island is conical in shape and averages ~ 7 km in diameter from the surface to 200 m, where the current speed of the Kuroshio is $>0.5\text{ m s}^{-1}$ (Chang et al., 2013). Otherwise, three seamounts stand on the submarine ridge, with their shallowest depth <250 m (green contour lines in Figure 1). Chang et al. (2016) observed trains of large Kelvin-Helmholtz billows (~ 100 m in amplitude) above the seamount, immediately to the northwest of Green Island, due to the Kuroshio flow interaction with the seamount. It is expected the seamount has insignificant influence on the Green Island wake because the Kuroshio often flows $15\text{--}30^\circ$ northeastward (Chang et al., 2018). In our model, the upstream current is 18° northeastward, depicted as white arrow in Figure 1.

Two in situ data sets were collected in the part of the Observations of the Kuroshio Transports and their Variability (OKTV) project sponsored by Taiwan's Ministry of Science and Technology. Both data sets were collected by the Taiwanese R/V *Ocean Researcher III* (OR3) (Figure 1). In the first survey (survey 1), 3 September 2013–6 September 2013, 12 repeated transects were conducted ~ 5 km downstream of Green Island (blue dashed line in Figure 1). The goal was to capture the variability of the wakes' vertical structures. The length of the transects were ~ 20 km; each transect took ~ 2 h to complete and was conducted nearly perpendicular to the wake direction. Measurements included the underway conductivity-temperature-depth (UCTD) and shipboard 75 kHz acoustic Doppler current profiler (ADCP). The range of the ADCP measurement was 17–489 m with a bin size of 8 m and with interval of 1 min. The underway CTD samples temperature, salinity, and pressure. In total, 226 UCTD casts were conducted during the 12 transect experiments. The resolution of the shipboard ADCP and the underway CTD along the transect was, respectively, below 0.12 and 1 km.

A second fast survey (survey 2) from 13 July 2014 to 16 July 2014 targeted in the area of anticyclonic recirculation immediately to the lee of Green Island (red line in Figure 1). A scenario of anticyclonic eddy formation was delineated. The experimental region was a rectangle measuring 7.2 km × 5.2 km. Each round took 3 h to complete, and the survey consisted of 10 consecutive loops. The key measurements were Shipboard ADCP, and the Underway Surface CTD (SCTD), focusing on the wake's surface variation. The spatial resolution of the ADCP was 0.12 km, and the SCTD was 0.16 km.

3. Numerical Model

3.1. Model Configuration

The Massachusetts Institute of Technology Ocean General Circulation Model (MITgcm) is widely used to study both large and small scale processes. The model solves the Navier-Stokes equation under the Boussinesq approximation. Primitive equations are written in z -coordinates and solved by the finite volume method (Marshall et al., 1997). The x axis and y axis are, respectively, positive east and north, and the z axis is positive up. The equations are:

$$\frac{D\bar{V}_h}{Dt} + f\hat{k} \times \bar{V}_h + \frac{1}{\rho_0} \nabla_z p = \bar{F} \quad (1)$$

$$g + \frac{1}{\rho_0} \frac{\partial p}{\partial z} = 0 \quad (2)$$

$$\frac{1}{\rho_0} \frac{D\rho}{Dt} + \nabla_z \cdot \bar{V}_h + \frac{\partial w}{\partial z} = 0 \quad (3)$$

$$\rho = \rho(\theta, S, p) \quad (4)$$

$$\frac{D\theta}{Dt} = Q_\theta \quad (5)$$

$$\frac{DS}{Dt} = Q_S \quad (6)$$

where $\bar{V}_h = (u, v, 0)$ is the horizontal component of velocity, w is the vertical velocity, $\frac{D}{Dt}$ is the total derivative, f is the Coriolis parameter, p is the pressure, \bar{F} is the frictional force, $g = 9.81 \text{ ms}^{-2}$ is the gravitational acceleration, and ρ_0 is the reference density. θ , S , and p are, respectively, the potential temperature, salinity, and pressure. Q_θ and Q_S are, respectively, the diffusions θ and S .

The model regime was a 285 m deep rectangle spanning 80 km × 80 km horizontally, from 121.3°E to 122.0°E zonally, and from 22.5°N to 23.2°N meridionally. The horizontal resolution is 500 m × 500 m throughout the whole domain. At the upper 35 m, the vertical grid size increases linearly from 5 to 9 m (1 m increment every grid), while the resolution is 10 m between 35 and 285 m (Figure 2a).

It is a free-surface model with nonhydrostatic capability. Nevertheless, we still utilize the hydrostatic formulation in our model. Open boundary conditions are applied for all four boundaries. The model is driven by a constant flow at all times, which only has vertical shear (Figure 2d). The inflow comes from the south and the west boundaries, while the outflow is to the north and the east. The flow velocity at the west, south, and east boundaries is identical. We calculate the flux of the input/output and control the outflow on the north boundary to balance the transport. Consequently, the flux on the north boundary is larger than the rest (black arrows in Figure 2a) and can prevent vertical compensation during the simulation. A constant heat at four of the boundaries is also given throughout the model run. The initial temperature and upstream flow conditions are, respectively, shown in Figures 2b and 2d, and are based on historical observational data. The flow was continuously stratified with a depth-dependent initial condition, whereas the salinity remained constant (Figures 2b and 2c).

A realistic topography is implemented to the domain with a resolution of 250 m (Ocean Data Bank, IONTU). Land masks are zeroed out, i.e., the eastern coast of Taiwan and Green Island were set to 0 m. No-slip boundary conditions were applied at the side and the bottom where the feature of the flow separation can be represented. The Coriolis coefficient f was set to a constant value of 10^{-4} s^{-1} . The boundary layer and the

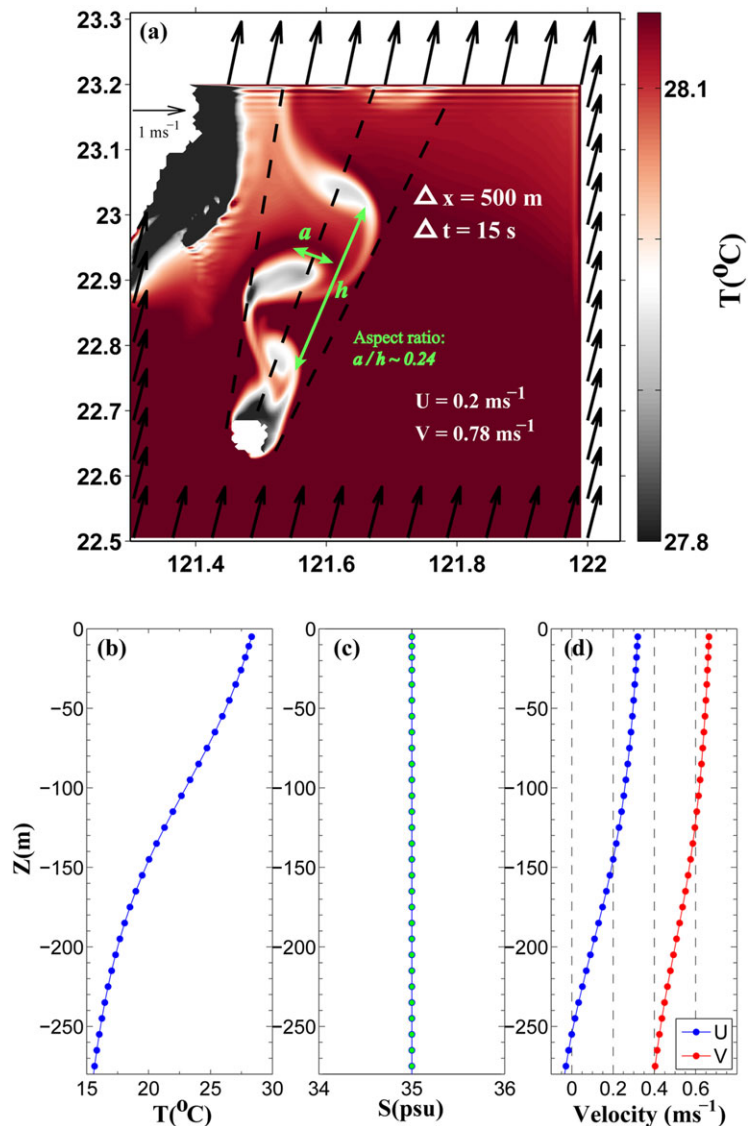


Figure 2. (a) The model domain for the Kuroshio pass Green Island in terms of the sea surface temperature. The $\Delta x = \Delta y$ was 500 m and the integration time step was 15 s. The zonal and meridional velocity are, respectively, shown as U and V . The given force is shown by the black vectors. The aspect ratio a/h is demonstrated by the ratio of the two green arrows. The initial condition of the (b) temperature profile, (c) salinity profile, and (d) zonal velocity (blue), meridional velocity (red) profiles.

downstream wave-like motion can be well resolved using the above settings, which allows us to investigate near-Green Island dynamics.

3.2. Eddy Viscosity and Advection Scheme

The horizontal eddy viscosity and the advection scheme for the temperature and the salinity should be carefully selected. The representation of the horizontal eddy viscosity (ν_H) in this study is the explicit horizontal eddy viscosity (ν_e) alone, which is associated with the physical diffusion processes. The implicit horizontal eddy viscosity (ν_i) is associated with the numerical diffusion, which is usually unavoidable. The effect of the numerical diffusion is similar to that of the physical diffusion and should be differentiated. However, the approach for quantifying the numerical diffusion is essentially a long-time problem.

This study investigates wake performances in terms of the application of various advection schemes, e.g., the third-order direct space time (DST) flux limiter scheme and the fourth-order central difference scheme. DST is a nonlinear advection scheme, which commonly produces additional numerical dissipation, and is often

difficult to quantify. To avoid the unknown implicit eddy viscosity (ν_i), we used the centered fourth-order scheme, which is a linear advection scheme. We expect the numerical diffusion can be reduced substantially as suggested in Tseng (2008). The explicit horizontal eddy viscosity is a constant Laplacian diffusion coefficient $\nu_e = 15 \text{ m}^2 \text{ s}^{-1}$, which is discussed in section 3. We apply the biharmonic diffusion of heat and salt laterally in the sense that it is more scale selective than the Laplacian diffusion and is less likely to diffuse away (Adcroft et al., 2011). The selection of the vertical diffusion coefficient is not completely based on physical considerations. To avoid excessive numerical dispersive effects, we choose a proper vertical diffusion coefficient, $10^{-3} \text{ m}^2 \text{ s}^{-1}$ as suggested by Gerdes et al. (1991).

3.3. Horizontal Resolution

The sensitivity of the horizontal resolution is investigated in idealized conditions, e.g., a cylinder island. The realistic topography may represent distinct island geometries in different resolutions, which might influence the flow separation and the resulting wake. We performed three experiments with the same configuration (not shown) but different grid resolutions, namely, 250, 500, and 1,000 m (respectively, from left to right in supporting information Figure S1a).

We performed a spectral analysis in the three different resolutions (supporting information Figure S1b) from day 10.4 to day 22.3 at 121.55°E, 22.85°N (black dot in supporting information Figure S1b), 20 m. The result shows that for a resolution of 1,000 m, the corresponding shedding period is ~ 14.84 h. As the grid resolution falls to < 500 m the shedding period remains constant at ~ 12.82 h. Furthermore, the resolutions of 250 and 500 m have similar spectrum variations. The wake behavior can be appropriately resolved by using the 500 m horizontal grid size. As a result, we apply this realistic condition in our model with a horizontal resolution of 500 m for further analyses.

4. Model Sensitivity and Validation

4.1. Effect of Advection Schemes

After the onset of the formation of the vortex street, the temporal variations of the wake flow can be expressed as the shedding period (T) of the continuous eddies to the lee of the island, which is related to the Strouhal number ($St = D/TU$). In general, the value of St is a function of Re . Previous cylindrical wake studies on the relation between St and Re were made via laboratory and numerical experiments (Coelho & Pinho, 2003; Coutis & Middleton, 2002; Huang et al., 2014; Williams, 1988; Williamson & Brown, 1998) and were summarized as the Re - St diagram shown in Figure 3a. The empirical formula derived by Williamson and Brown (1998) (black curve in Figure 3a) indicates that the value of St is positively related to the value of Re , and rapidly increases from 0.12 to 0.22 in $50 < Re < 400$ and gently increases from 0.22 to 0.24 in $400 < Re < 1,000$. The other experiments (i.e., Coelho & Pinho, 2003; Coutis & Middleton, 2002; Huang et al., 2014; Williams, 1988) show trends very similar to Williamson and Brown (1998). Note that only the case of 0.2% tylose solution in Coelho and Pinho (2003) is shown here. Accordingly, given that the diameter of the cylinder and the horizontal eddy viscosity is constant, the stronger incoming flows lead to a shorter shedding period. We will borrow the diagram to examine whether the Green Island wake is characterized by the VKVS. Detailed physical explanation of the Re - St diagram (or Williamson-Brown curve) can be found in Williamson (1996).

To compare our model with those previous numerical modeling results, numerical simulations using $Re = 60$, $Re = 80$, $Re = 95$, $Re = 190$, $Re = 315$, $Re = 590$, and $Re = 945$ were conducted in terms of the third-order DST flux limiter and centered fourth-order temperature/salt advection scheme. The island diameter ($D = 7$ km) and the upstream velocity ($U = 0.675 \text{ m s}^{-1}$) are given as constants, thus Re only varies by ν_H . We applied spectral analysis of zonal velocity at 121.55°E, 22.75°N to estimate the shedding frequency, and were then able to calculate Re and St . It is found that the cylinder island wake in our model has a similar Re - St trend with previous experiments when $Re > 200$ in both the third and fourth temperature/salt advection schemes, which appeared as a nearly constant value of $St \sim 0.22$ (red solid and dashed lines in Figure 3a). This result roughly agrees with Dong et al. (2007), indicating that the St remains ~ 0.23 in $100 < Re < 6,400$. However, St is considerably higher than the predicted curve when $Re < 200$.

For an island wake in realistic geometry, the value of St is ~ 0.02 – 0.044 higher than in a cylinder wake in both mixing schemes (solid blue and dashed blue curves). The results suggest the key discrepancy when an

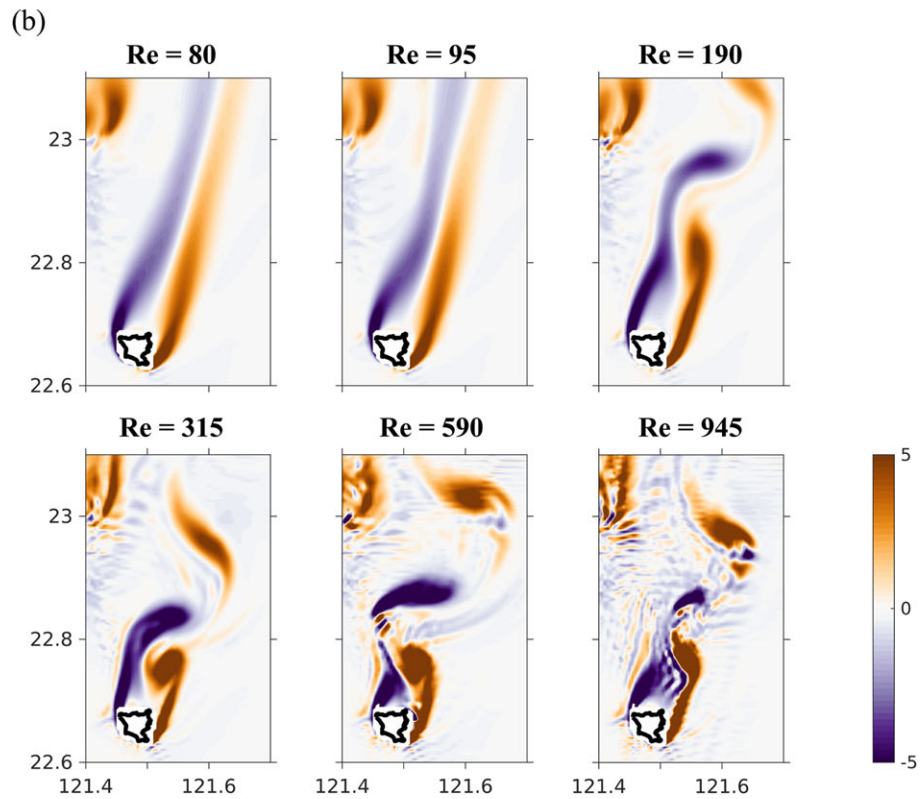
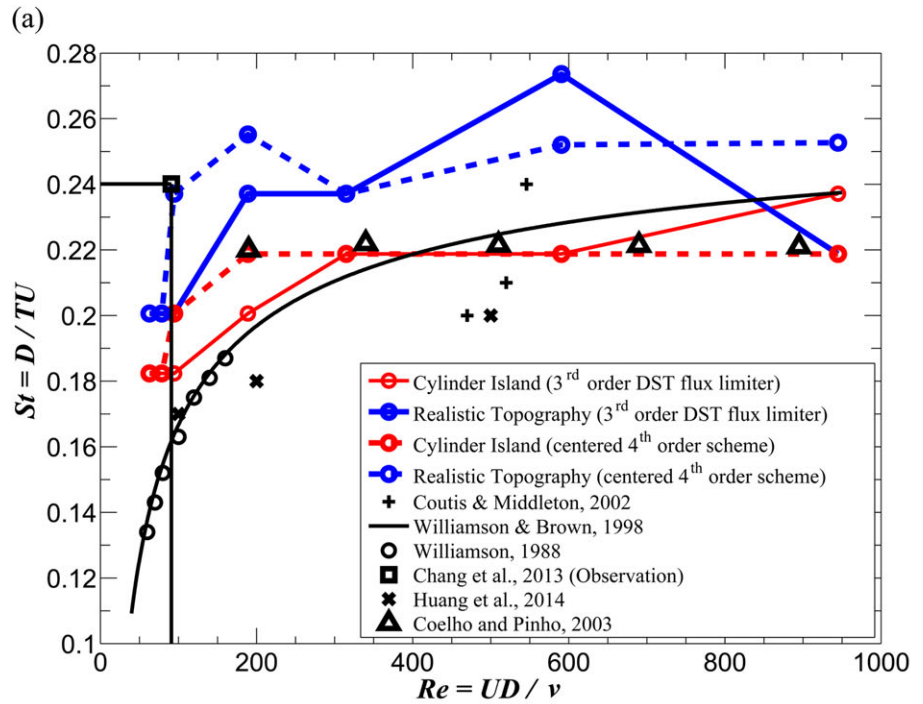


Figure 3. (a) Model results presented by Strouhal number (St) versus Reynolds number (Re) diagram. Red and blue lines are, respectively, the cylinder island (CI) and the realistic topography (RT). The colored solid lines are under the third-order DST flux limiter scheme, and the colored dashed lines are the centered fourth-order scheme. Black crosses (+), triangles (Δ), and circles (O) represent the cylinder experiments from previous studies. Black crosses (x) are the results from Green Island simulated by the numerical model. The solid black line is the empirical curve. The square symbol (\square) is the field observational results at Green Island. (b) Normalized surface vorticity (ζ/f) patterns when $Re = 80, 95, 190, 315, 590,$ and 945 , using centered fourth-order advection scheme on day 8.6.

idealized cylinder island replaces the realistic geometry of the island in the numerical model. Field observations conducted by Chang et al. (2013) inferred that $Re \sim 91$, where $v_H \sim 100 \text{ m}^2 \text{ s}^{-1}$. Furthermore, $St \sim 0.24$ according to our model results with fourth-order schemes in RI (Figure 3a).

According to Figure 3a, using either the third-order DST flux limiter scheme or the centered fourth-order scheme, the shedding frequency is analogous when $Re < 100$. Nonetheless, once the $Re > 100$, the third-order (solid lines) and the fourth-order (dashed lines) schemes have different St . This is possibly because the diffusion in the third-order scheme is more significant than the fourth-order scheme (section 3.2), especially when $Re > 100$. Consequently, irregularity of the St in the third-order scheme is notable. On the other hand, the fourth-order scheme almost converges to a constant St when $Re > 300$, which tends to be more similar to the trend of previous numerical and water tank experiments. Possibly, the use of the centered fourth-order scheme is recommended to simulate the island wake.

4.2. Dependency of Wake Pattern on Reynolds Number

It seems that $Re = 91$, corresponding to $St = 0.24$ in the Re - St diagram, is a preferred setup for our model. However, further analyses are needed because the implicit viscosity (ν_i) in our model is unknown and the value of Re suggested in Chang et al. (2013) is a rough inference. The wake patterns as a result of different Re by using centered fourth-order advection scheme (Figure 3b) are shown as the normalized vorticity (ζ/f). The wake behaviors depend significantly on Re . Numerous small wiggles appear in the model domain, especially when the value of Re is 315, 590, and 945. This is because the centered fourth-order scheme is dispersive and leads to unsteadiness when Re is large. The vortex-like pattern is absent when $Re = 80$ and $Re = 95$. Instead, two elongated positive and negative vorticities, resembling vorticity tails, appear to the lee of the island. The vortex street-like structures become clearer and the magnitude of vorticity becomes stronger from $Re = 190$ to $Re = 945$. The vorticity tails were found to slightly swing in the cross-wake direction at a fixed period. Therefore, the values of St in Figure 3a when $Re = 60, 80, \text{ and } 95$ are related to the swinging period of the vorticity tail, instead of the shedding period of the eddy. Clearly, $Re = 91$ is not a suitable choice in our simulation since the eddy shedding process is not present. To determine a reasonable model setup, we further compare our model results with field observations in the next section.

4.3. Comparison With Field Observations

Previous analysis of the dependency of St on Re revealed the shedding period (T) changed with different values of Re in our model setup. However, a realistic Re value is unobtainable because the horizontal eddy viscosity is unknown. Moreover, the numerical diffusion in the model is unclear. Therefore, two field experiments were used to validate our model and to determine the value of Re in our model. From the surface manifestation (Figure 3b) and the shedding period of the wake (Figure 3a) in observations, $Re = 315$ may be a reasonable value for the Green Island wake simulation.

In the first survey, the results were summarized as the longitude-time contours of the zonal velocity, meridional velocity, and temperature at 20 m, and are, respectively, shown from the left to right plots in Figures 4a and 4b. The longitude-time contours of zonal velocity show the eastward and westward flows alternately appeared within a 25 h duration, which indicate the prevalence of the cyclonic and anticyclonic recirculation, respectively. The meridional velocity shows a wave-like return flow (negative velocity) at a current speed of $\sim 0.5 \text{ m s}^{-1}$, related to the shoreward flow of the recirculation. The return flow is roughly accompanied with colder water, with temperatures $\sim 1^\circ\text{C}$ lower than the adjacent water. Field observations revealed a wake period of $\sim 12 \text{ h}$, as marked by double head arrows (Figure 4b). For further comparison, the numerical results with the setting of $Re = 315$ at the same transect were abstracted and shown to have similar longitude-time contours (Figure 4a). The results of the numerical model agree well with observations, especially for zonal velocity. The meridional velocity and temperature in observations reveal patterns similar to the numerical model, but not as clear as that in zonal velocity. Hereafter, $Re = 315$ will be used for the wake simulation.

In survey 2, the surface pattern of the wake immediate to the lee of the island was investigated. A sequence of experiments was conducted with an interval of 2.5–3 h (Figure 4d). The numerical model and the observations revealed a similar wake pattern. A complete cycle of the evolving recirculation ($\sim 12 \text{ h}$) was captured in Figures 4c and 4d. Initially, the Kuroshio detours from the west flank to the northeast of the island, forming an anticyclonic recirculation. Subsequently, the recirculation departed downstream to the northeast.

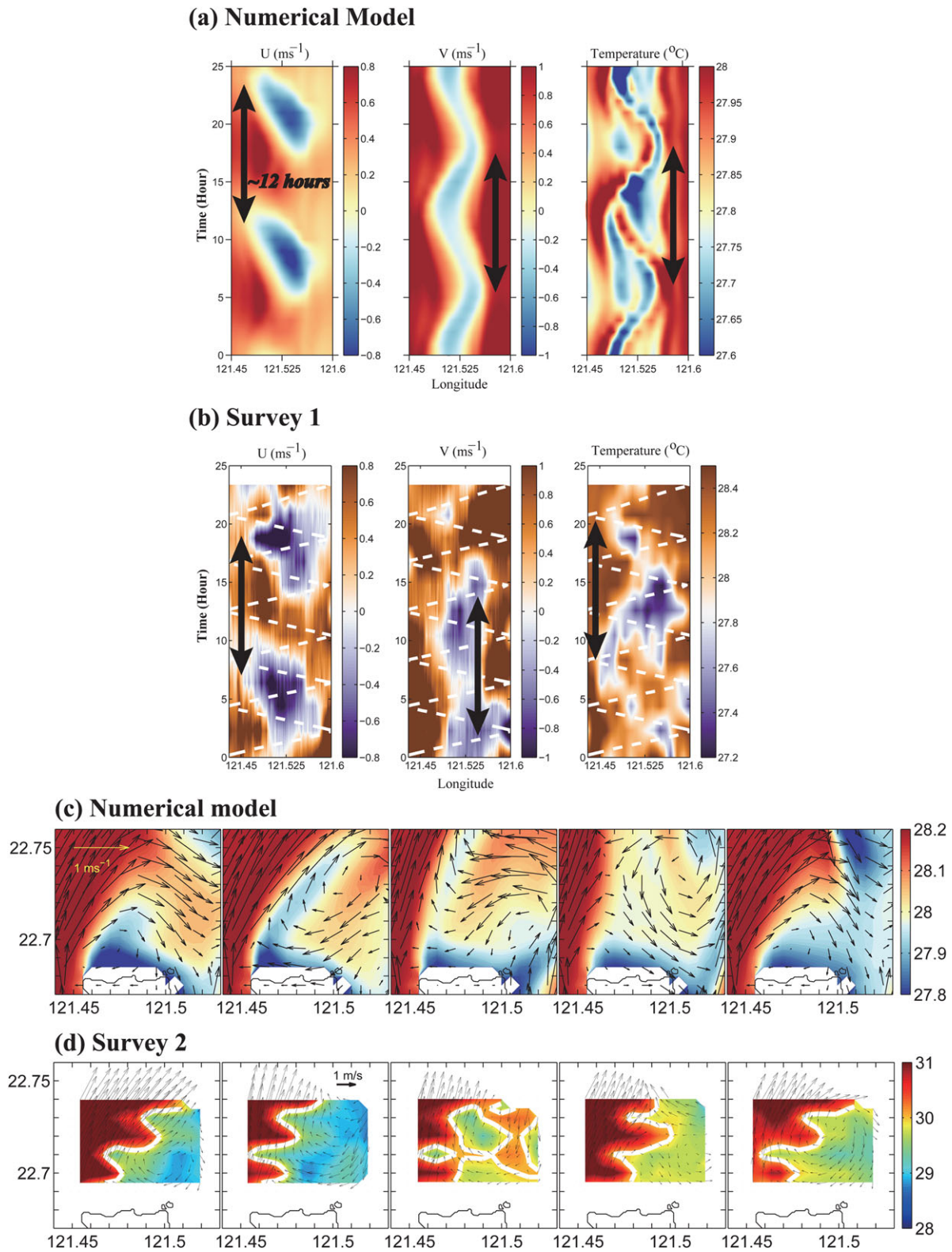


Figure 4. (a) and (b) are the numerical and the field observation (survey 1) results. The longitude-time contour of zonal (U), meridional (V) velocity, and temperature at the cross-wake transect (the blue line in Figure 1) are represented from the left to right. The double-arrow lines represent the duration of one shedding period. The white dashed lines are the ship tracks. Surface temperature and velocity vectors are depicted by the (c) numerical model and (d) the quasi-synoptic surface temperature and velocity vectors in survey 2. Note that the time interval of each figure is 3 h.

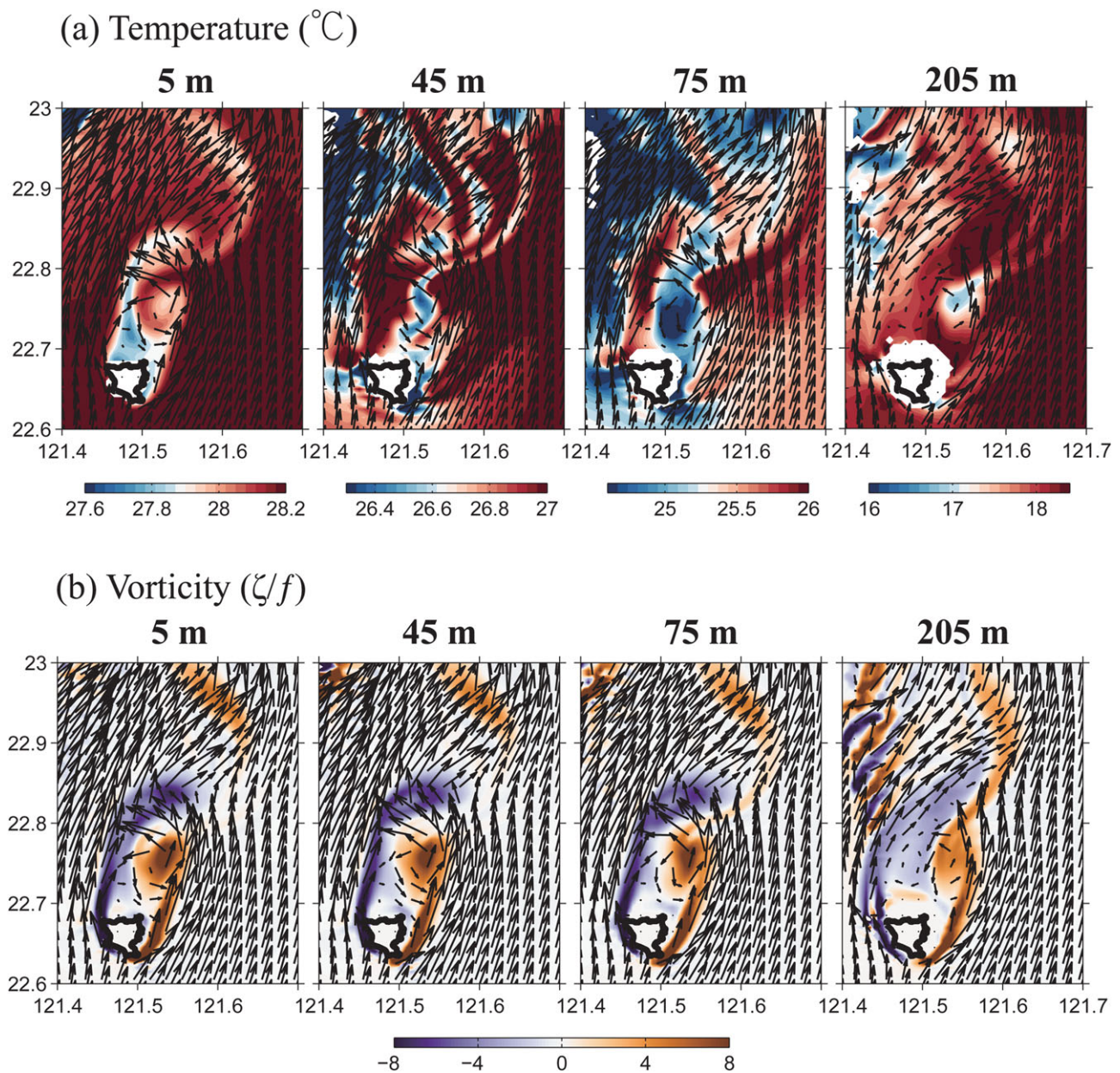


Figure 5. Plane view of the Green Island wake at different depths (5, 45, 75, and 205 m) with respect to (a) temperature and (b) normalized vorticity on day 8.6. Vectors indicate velocity. The black line is the island's coastline.

Meanwhile, the current on the eastern flank rose and developed a cyclonic recirculation, gradually propagating downstream. Thereafter, the current on the west flank dominated once again and detoured clockwise to the lee of Green Island. The observations resolved the process of eddy shedding and validated our model.

5. Results

5.1. Plane View and Vertical Structure

The plane view of the wake was investigated in terms of temperature distribution (Figure 5a) and normalized vorticity (ζ/f) (Figure 5b) at the lee of the island on day 8.6. Different layers show distinct wake patterns presumably due to the island-shelf effect and the vertically varied upstream velocity. Clearly, the area and magnitude of the recirculation become, respectively, larger but weaker with the increase of the depth (Figure 5b).

The correspondence between high vorticity and low water temperature is different near the surface than in deeper water. The cold water in the cyclonic (121.52°E, 22.75°N) and anticyclonic (121.53°E, 22.83°N) recirculation is presumably related to the upwelling process, since the influential depth of the upwelled cold water is over 100 m (Figure 5a). This suggests the upwelling is not primarily a geostrophic dynamic since the negative vorticity favors the downwelling in the geostrophic balance. However, the cold water from the anticyclonic recirculation is clearly smaller in range and less significant than the cyclonic recirculation, especially at deeper layers, e.g., >45 m. It is expected that the asymmetry of temperature drop response is associated with the inertial instability that favors the survival of cyclonic eddies and destabilizes or breaks anticyclonic eddies. The impact of inertial instability is further discussed in section 5.3.

In addition to upwelling, parts of the cold water in both recirculations at shallow region (<45 m) are sourced from the cold water immediate to the lee of the island by horizontal advection, forming a vortex-tail pattern. Apart from the cold water, the water on the western flank of the wake is warmer than its surroundings, roughly at 45–200 m. A possible mechanism for the rise of warm water in this frontal region is the overturning and mixing process, which is presumably associated with vertical shear. Further details of the mechanism of the vertical shear will be discussed in section 5.5.

Survey 1 provided information on the wake's vertical structure wake. However, the field observations are inadequate to delineate the wake downstream. Therefore, we conduct four transects in our model to identify different vertical structures at different distances from the island. Three cross-wake transects L1–L3 (~23.5 km) and one along-wake transect L4 (~35 km) are shown in Figure 6a. Temperature, along-wake velocity, and vorticity were investigated along the four transects (supporting information Figure S6b). L1 reveals uplifting of the isotherms. The consequence of the uplift of isotherms implies vertical mixing and/or upwelling. The isotherm dome is about 50 m deep at the region where the southwestward flow is located, which is also in between the strong positive and negative vorticities. A cyclonic recirculation temporarily passes L1, which increases the breadth of the uplift isotherm (~10 km).

About 5 km away from L1, L2 shows a vertical structure similar to that of L1, but at the northern edge of the cyclonic recirculation. Consequently, a stronger upstream velocity can be seen on the wake's western flank, but the positive vorticity weakens significantly at the upper 50 m. Even further downstream to L3, the anticyclonic recirculation is adjacent to L3. Thus, it is expected that the negative vorticity dominates, and the southwestward flow is weak. The cold dome at the L3 transect is not as significant as at L1 and L2. Nonetheless, possible overturn may happen at a depth of 100 m, which is possibly associated with the vertical front. L4 is the only along-stream transect. Isotherm uplift also occurs in the region of the cyclonic recirculation to the very north of L4 (vorticity tail). It crosses both the cyclonic and anticyclonic recirculation. At the first 15 km, the flow is predominantly southwestward due to the cyclonic recirculation. On the other hand, the flow is predominantly northeastward at 15–35 km.

5.2. Von Kármán Vortex Street

We examine the wake evolutions from the model output in the following section. The von Kármán vortex street (VKVS) is a phenomenon where a flow past an obstacle causes the attached eddies to periodically be shed from the obstacle, forming staggered vortices downstream. It occurs at a certain Re range, i.e., $80 < Re < 200$ (Kundu et al., 2012). Given the geophysics of the Green Island wake scenario (rotational and stratified flow), the transition regime of the Re values are larger, namely, $150 < Re < 500$. However, the trend of the St versus Re curve in the Green Island wakes is nearly identical to that of cylinder laboratory experiments (Figure 3a). This indicates that, in the transition regime, the shedding frequency of the classical VKVS shares similar tendencies with the Green Island wake scenario.

The characteristics of the Green Island wakes depend on Re (Figure 3b), which demonstrates features analogous to the Kármán vortex street. In the VKVS, when the adverse pressure gradient is attained, the flow separates from the boundary and forms the wake; Green Island wakes show a similar mechanism (not shown). von Kármán and Rubach (1912) found that local circulations are theoretically stable when they satisfy a certain aspect ratio. This stability gives the vortex streets the potential to retain their vorticity in the wake zones for a fairly long distance. The characteristics of a classical VKVS are determined by quantitative metrics, e.g., the aspect ratio (von Kármán & Rubach, 1912) and the dimensionless width (Nunalee & Basu, 2014). According to von Kármán's linear first-order stability theory for inviscid flow around a cylinder, the aspect

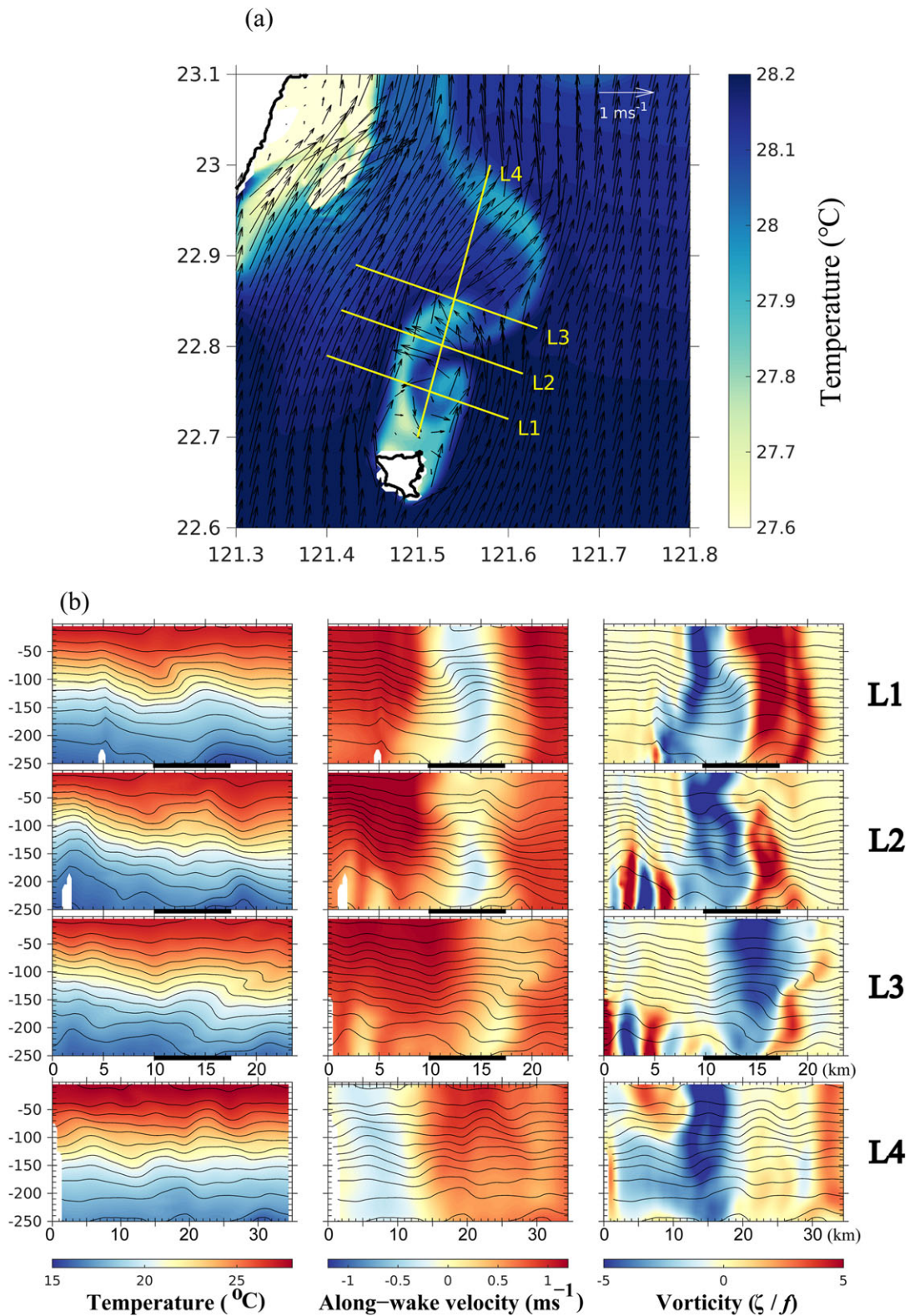


Figure 6. (a) Snapshots of SST and velocity vectors on day 8.6. L1–L3 are the cross-wake transects, L4 is the along-wake transect for investigating the vertical structure. (b) Distance-depth contour of temperature (left column), along-wake velocity (middle column), and normalized vorticity (right column) on day 8.6 along transects L1–L4 (Figure 6a). Black contours show the isotherms from 15°C to 29°C with a 1°C interval. Thick black lines at the bottom of L1–L3 are the horizontal extent of Green Island projected onto each transect.

ratio (h/a) is 0.281, where h is the distance between two vortices on different rows, a is the distance between two vortices on identical rows (Figure 2a). On the other hand, the dimensionless width (h/D) observed in the laboratory is 1.2 (Nunalee & Basu, 2014). The metrics in our model are estimated to have an aspect ratio of ~ 0.24 and a dimensionless width of ~ 1.11 (Figure 2a). Though the variability of the upstream current speed, temperature, and the length scale, viscosity, etc. is far from laboratory conditions, our values of the metrics are still in the same order as the laboratory results, indicating that, in a complex geophysical system, island wakes are similar to a Kármán vortex street. Otherwise, the slight discrepancy from the $St-Re$ relationship and the aspect ratio in the wake of Green Island may imply additional physical processes need to be considered.

5.3. Inertial Instability

In geophysical flow, rotation tends to stabilize parcels with respect to horizontal displacements. Instability with respect to horizontal displacements is referred to as inertial instability, with a necessary condition of $f(f + \frac{\partial v}{\partial x}) < 0$ in the northern hemisphere (Holton, 1992). This suggests that the inertial instability occurs in a wake region where the relative vorticity is negative and its magnitude is larger than planetary vorticity f . Figure 5b shows that inertial instability could occur in the anticyclonic recirculation where $|\zeta/f| > 1$. The inertial instability would destabilize or break the anticyclonic recirculation and eventually weaken the negative vorticity. Therefore, it is expected that the magnitude of the positive vorticity is larger than the negative vorticity.

To further clarify the effect of inertial instability, following Dong et al. (2007), we track a pair of cyclonic (day 8.4–9.0) and anticyclonic (day 8.5–9.1) recirculations and record their maximum vorticity (supporting information Figure S2) at 5 m. The initial time (1 h) for both the cyclonic and anticyclonic recirculations are determined by the time at which the recirculation is fully developed, when the vorticity magnitude no longer increases. Thereafter, both recirculations propagate downstream, and quickly decline due to diffusion. The normalized vorticity magnitude of the anticyclonic eddy is clearly smaller than the cyclonic eddy from the beginning to the end, possibly because the inertial instability distorts the anticyclonic eddy and results in a relatively weaker vorticity magnitude.

Two experiments were designed to investigate the dependency of the Coriolis parameter and the upstream flow magnitude on the island wake behaviors. In the first experiment, we set the Coriolis coefficient f to 10^{-4} s^{-1} (Figure 7a) and 0 s^{-1} (Figure 7b) in terms of the surface distribution of the normalized vorticity on day 8.6, 5 m. When $f = 10^{-4} \text{ s}^{-1}$, both the size of recirculation and the normalized vorticity magnitude are smaller than when $f = 0 \text{ s}^{-1}$. This is because the rotation destabilizes parcels in terms of horizontal displacements. Furthermore, the existence of the Coriolis effect is essential for the inertial instability to grow. The imbalance between the local pressure gradient and the Coriolis force leads fluid particles away from their original position. The instability is invalid without the Coriolis effect.

We conduct the second experiment to understand the dependency on upstream velocity. The upstream velocity in Figures 7c and 7d are, respectively, selected as 0.675 and 0.255 m s^{-1} . Note that the scenario in Figure 7a is identical to that in Figure 7c, but with a different color scale. The results show that once the relative vorticity weakens to $< 3f$ (Figure 7d), the anticyclonic recirculation scatters more than when the vorticity is $10f$ (Figure 7c). According to the frequency of the inertial instability $\omega = \sqrt{f(f + \frac{\partial v}{\partial x})}$, the growth rate of the inertial instability will increase with the negative vorticity magnitude, and fluid particles are more prone to move outward. Nonetheless, the inertial instability does not cause significant distortion to the anticyclonic recirculation (Figure 7c) as the case in Dong et al. (2007) or Chavanne et al. (2010). This is possibly because strong horizontal shear leads to a strong outward force on the particles. Hence, in the anticyclonic recirculation, the outward force tends to turn right because of the Coriolis effect, and eventually spins clockwise to consolidate the structure of the anticyclonic eddies. Weak negative vorticity magnitude has a weak outward force, producing destructive anticyclonic recirculation (note that the relative vorticity magnitude still has to exceed $1f$).

Herein, we also evaluate the possible occurrence of symmetric instability, which could happen in baroclinic flows and can therefore be interpreted as inertial instability in the isopycnal surface. It considers not only the inertial instability but also the gravitational instability. For instability to the following must be satisfied:

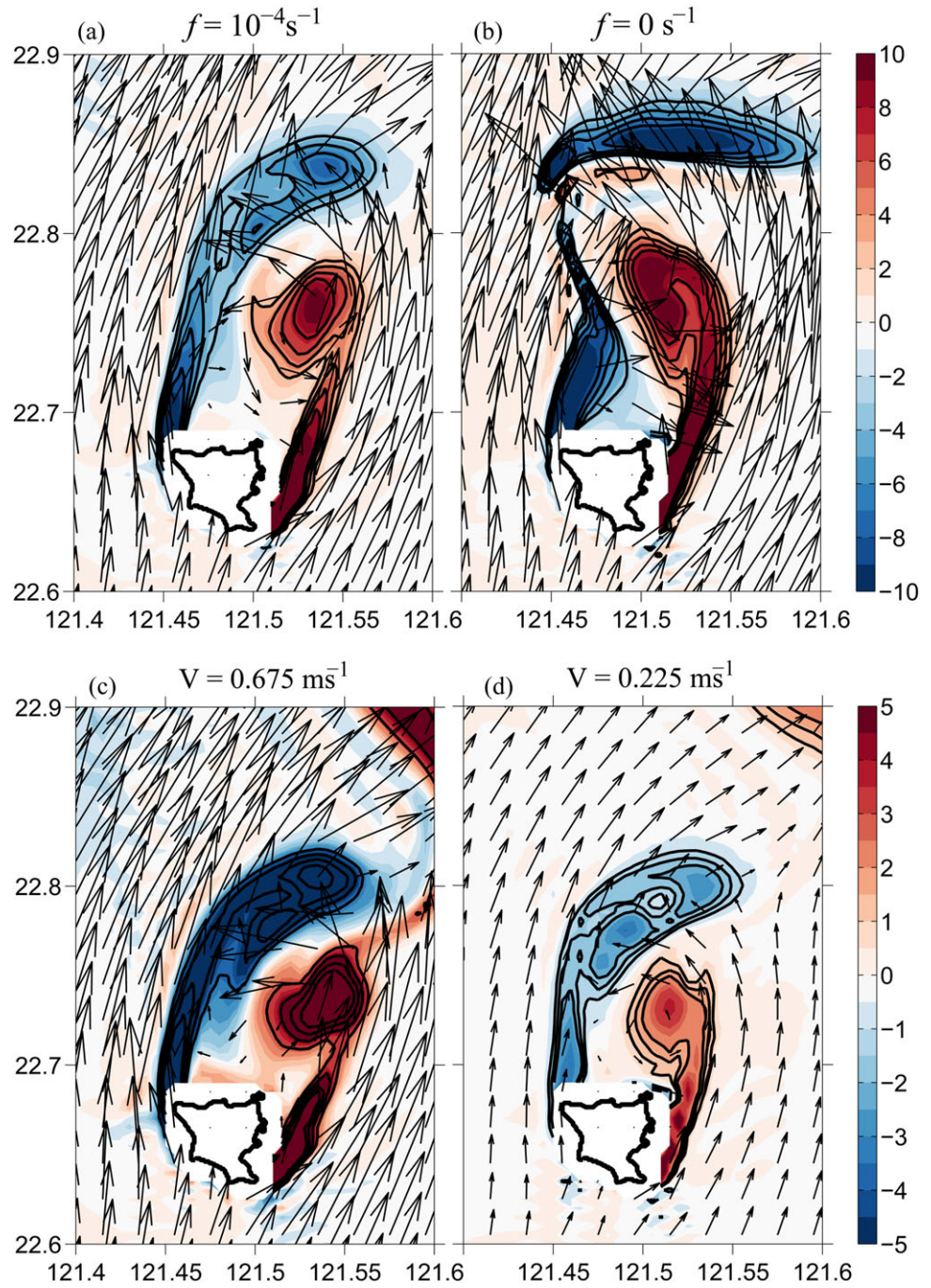


Figure 7. The surface vorticity (normalized by $f=10^{-4} \text{ s}^{-1}$) on day 8.6. (a) $f=10^{-4} \text{ s}^{-1}$ and (b) $f=0 \text{ s}^{-1}$. The effect of the centrifugal instability only occurs at the anticyclone (left plot). The influence of the upstream velocity on the wake performance (c) 0.675 and (d) 0.225 m s^{-1} . It shows the centrifugal instability becomes notable when the vorticity is smaller.

$$F^2 N^2 < f^2 M^2, \quad (7)$$

where

$$F^2 = f \left(f + \frac{\partial v}{\partial x} \right); \quad N^2 = \frac{-g}{\rho_0} \left(\frac{\partial \rho}{\partial z} \right); \quad fM = f \frac{\partial v}{\partial z}.$$

The criterion (7) means that the density slope is steeper than the momentum slope (Cushman-Roisin & Beckers, 2009). The estimation of the criterion (7) suggests that symmetric instability is not preferable in the Green Island wake scenario (not shown). The stratification characteristic is perhaps another reason for why the lack of clear inertial instability in Green Island wakes. We conducted a weak-stratified case, where the surface is only 2°C higher than the bottom. The result shows more significant anticyclonic recirculation distortion than in the well-stratified scenario (not shown), suggesting that stratification increases the barrier to achieving instability.

5.4. Barotropic Instability and Baroclinic Instability

To explore the importance of the barotropic and baroclinic energy conversion in the von Kármán-like wakes, we examine the horizontal Reynolds stress (*HRS*) and the vertical buoyancy flux (*VPF*) in energy budget equation for the eddy kinetic energy (Gula et al., 2015; Kang & Curchitser, 2015). The estimation of the two terms allows us to quantify the importance between the eddy and mean flow interaction (e.g., Gula et al., 2015). The horizontal Reynolds stress ($HRS = -\overline{u_i u_j} \frac{\partial U_i}{\partial x_j}$, $i=1, 2, 3$; $j=1, 2$) and the vertical buoyancy flux ($VPF = \frac{g}{\rho_0} \overline{u_3' \rho'}$) are the conversion from the mean flow to eddy kinetic energy and the conversion from the eddy potential energy to the eddy kinetic energy, respectively. When $HRS > 0$, it indicates the eddy generation mechanism is predominantly a barotropic instability, whereas $VPF > 0$ may indicate a baroclinic instability (Gula et al., 2015).

Figures 8a and 8b are the time-averaged of *HRS* and *VPF* integrated over depth (5–205 m), respectively. Clearly, $HRS \gg VPF$ in the wake zone, suggesting the effect of barotropic instability is more important than baroclinic instability. Furthermore, the relationship between VKVS and barotropic instability is critical, where both mechanisms could contribute to sizable *HRS*. At the near-island region, positive *HRS* emerges at the separation point of VKVS adjacent to the island. *HRS* variability is small. Nonetheless, *HRS* variability is large at downstream region. Figures 8c and 8d show the combination of surface normalized vorticity distribution and depth-integrated *HRS* (black contour) from $-1-7 \text{ J m}^{-2} \text{ s}^{-1}$ with an interval of $2 \text{ J m}^{-2} \text{ s}^{-1}$ respectively on day 8.6 and 8.75. Clearly, both cyclonic and anticyclonic eddies do not overlap the regions of positive *HRS*; moreover, when eddies propagate away, *HRS* emerges after an hour. This suggests that positive *HRS* at downstream is a result of barotropic instability rather than VKVS. Barotropic instability serves as a secondary process for extracting energy in the shear layer and converting it into eddy kinetic energy. However, once the von Kármán vortices pass through, they undermine the maintenance of the shear layer condition for barotropic instability. Consequently, vortices and positive *HRS* are formed in a staggered manner.

The quantification of two conversion terms shows that *HRS* is generally larger than *VPF*, implying that the barotropic instability could play a role under the VKVS eddy generation process but the effect of baroclinic instability may be negligible. *Bu* is another useful measure for the possibility of barotropic and baroclinic instability. In our case, *Bu* is ~ 24 , much larger than 1, favoring the occurrence of barotropic instability.

5.5. Vorticity and Vertical Shear

Chang et al. (2013) reported CTD profiles in the island wake region revealed strong TKE dissipation rate of $O(10^{-7} - 10^{-5}) \text{ W kg}^{-1}$ relating to the shear instability. The vertical shear is responsible for the active overturning. In our model, the emergence of warm water at the west border of the wake could be a sign of overturning processes (section 5.1). We examine the generation of the vertical shear in the wake. First, the Green Island's conical shape may produce the vertical shear, i.e., considering the no-slip boundary condition, the flow weakens when it approaches the boundary, producing vertical shear adjacent to the island. Second, the vertical shear may be induced by the tilting of the vertical vorticity. The zonal vorticity component is investigated in this study. The governing equation for the zonal component of vorticity is:

$$\frac{\partial \zeta_x}{\partial t} + \vec{v} \cdot \nabla \zeta_x = - \left(\frac{\partial u}{\partial y} \frac{\partial w}{\partial x} - \frac{\partial u}{\partial z} \frac{\partial v}{\partial x} \right) - (\zeta_x) \left(\frac{\partial v}{\partial y} + \frac{\partial w}{\partial z} \right) + \frac{1}{\rho^2} \left(\frac{\partial p}{\partial z} \frac{\partial \rho}{\partial y} - \frac{\partial p}{\partial y} \frac{\partial \rho}{\partial z} \right) \quad (8)$$

which neglects the friction effect, and

$$\zeta_x = \frac{\partial w}{\partial y} - \frac{\partial v}{\partial z} \quad (9)$$

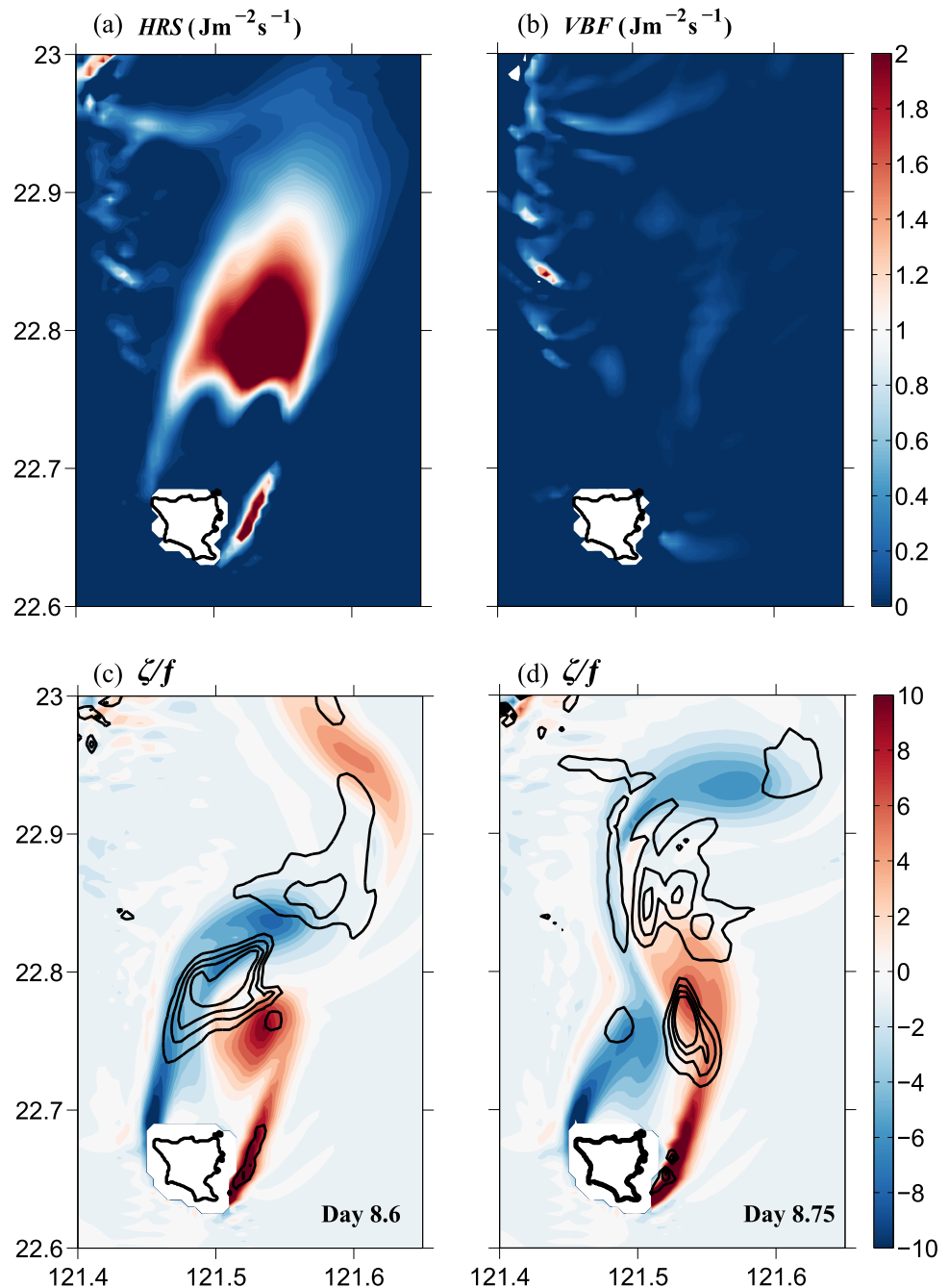


Figure 8. Plane view of the distribution of the vertically integrated time-averaged (a) horizontal Reynolds stress (HRS) and (b) vertical buoyancy flux (VBF) around the Green Island. (c) and (d) show the normalized vorticity respectively on day 8.6 and 8.75. Black contours are the integrated HRS value from $1-7 J m^{-2} s^{-1}$ with an interval of $2 J m^{-2} s^{-1}$.

The terms in (8) from left to right are, respectively, the vorticity tendency, advection (Figure 9a), vortex tilting (Figure 9b), vortex stretching (Figure 9c), and baroclinic term (Figure 9d). The estimation of each term in our model effectively explains the vorticity generation. Figures 9a–9d show the distribution of zonal vorticity terms integrated in 5–205 m. The advection term clearly dominates all the other terms and the baroclinic term is almost negligible ($10^{-11} s^{-2}$). The tilting and stretching terms are both noticeable, but we mainly focus on the tilting effect. In the tilting term, strong negative and positive values imply that the vertical vorticity (ζ_z) has tilted westward and eastward.

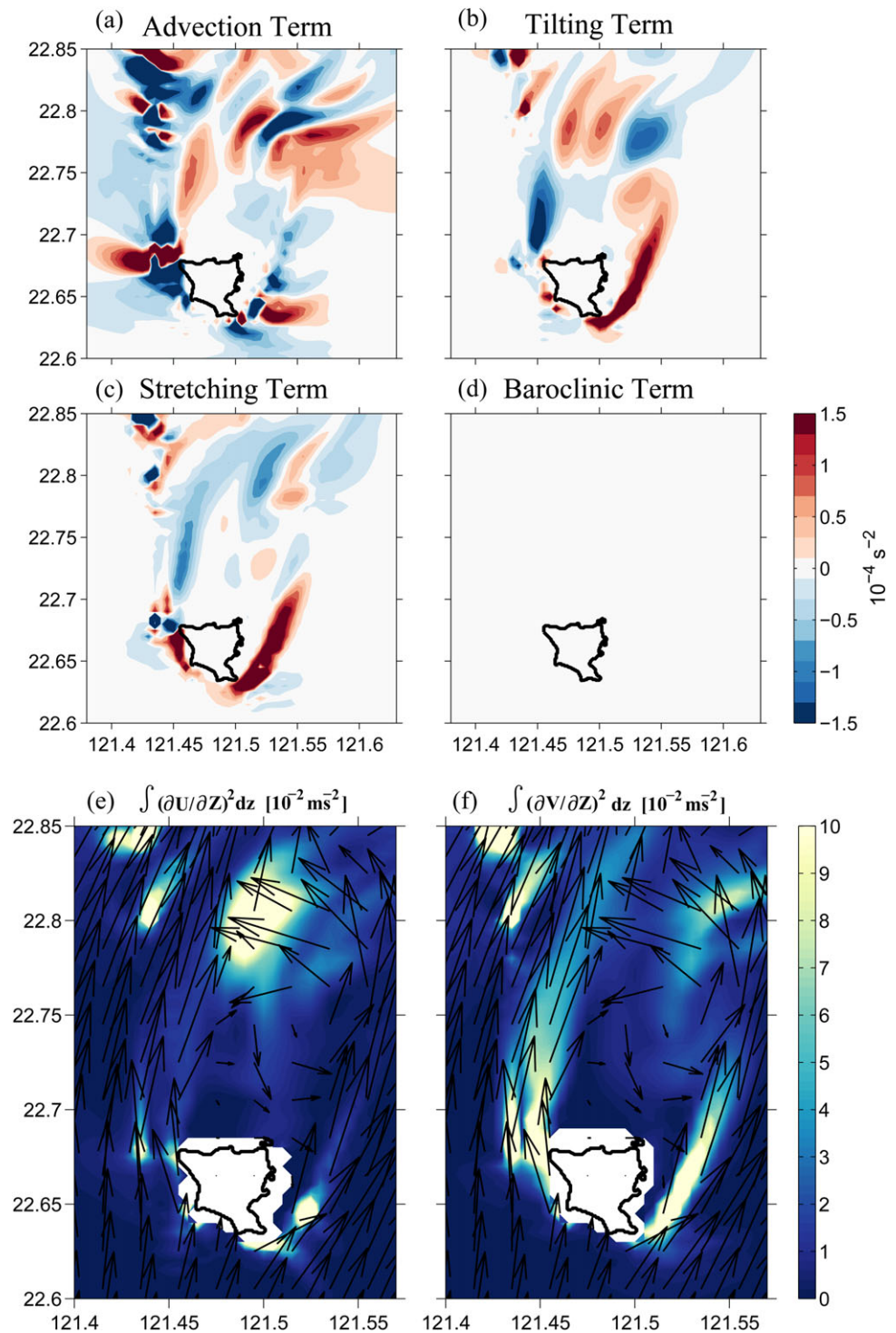


Figure 9. Plane view of the vertically integrated distribution of (a) advection term, (b) tilting term, (c) stretching term, (d) baroclinic term in the zonal vorticity equation, (e) $\frac{\partial U^2}{\partial z}$, and (f) $\frac{\partial V^2}{\partial z}$ on day 8.6.

A schematic diagram (supporting information Figure S3) shows the zonal tilting effect. When the vertical vorticity component (induced by $\partial v / \partial x$, solid red arrow) is tilted by $\partial u / \partial z$ (thick blue arrows), it subjoins the zonal component and produces vertical shear ($\partial v / \partial z$).

For the sake of simplicity, the cylinder island scenario is also investigated (not shown). We found that since the cylinder is vertically uniform, there is no island-shelf effect that produces sizable vertical shear ($\partial u/\partial z$ or $\partial v/\partial z$) at the boundary layer. However, the result still shows a strong tilting effect in the zonal vorticity component, $-\left(\frac{\partial u}{\partial y} \frac{\partial w}{\partial x} - \frac{\partial u}{\partial z} \frac{\partial v}{\partial x}\right)$, since $\partial v/\partial x$ is generally large because of the strong lateral shear in the boundary layer. Interestingly, significant tilting effect only happens in the zonal component (no signal is found in the meridional nor vertical components). This means that the lateral shear can be converted to meridional vertical shear by the tilting effect. The Green Island wake scenario should consider the island-shelf effect, where the vertical shear is no longer small ($\partial u/\partial z$ or $\partial v/\partial z \neq 0$). Figures 9e and 9f show the vertically integrated $(\partial u/\partial z)^2$ and $(\partial v/\partial z)^2$ from 5 to 205 m. The tilting effect of the meridional vorticity component is weaker, since $\partial u/\partial y$ is smaller than $\partial v/\partial x$ (not shown), consequently, $\partial u/\partial z$ will be less effectively produced by the tilting effect than $\partial v/\partial z$. Both zonal and meridional directions of the tilting effect are critical to the conversion of lateral shear to vertical shear. The vertical shear could drive overturning and mixing, and could explain the strong dissipation to the north of Green Island.

6. Conclusion and Discussion

Field observations show Kuroshio-induced wakes to the lee of Taiwan's Green Island. Regarding the spatial and temporal limitations of field observations, numerical simulations in the study help improve our understanding of wake evolution and dynamics. We analyze the properties and the dynamics of island wakes using the MITgcm. Model sensitivity tests, including variation of island geometry, horizontal diffusion, advection scheme, and horizontal resolution, help extract a suitable model configuration. Comparison between the field observations and the model shows similarities with respect to the shedding period (~12 h) and the near field pattern of the wake.

Green Island wakes resemble a typical VKVS. The behavior of the wake transition regime greatly depends on Re , and the relation between the shedding frequencies and the eddy viscosity coincides well with previous studies. The flow is separated from the boundary, forming a row of staggered vortices. The aspect ratio is similar to the Kármán's ratio as well. These characteristics of Green Island wakes demonstrate that they are VKVS. However, our model results show asymmetric development between cyclonic and anticyclonic eddies, i.e., the anticyclonic eddies were weakly distorted due to the inertial instability as claimed by Chang et al. (2013). Substantial temperature drops in the model appear only in the cyclonic recirculation and eddy in deeper water. The growth rate of the instability is large but the distortion of the anticyclonic eddy is not as significant as in previous findings (Dong et al., 2007). A strong restoring force consolidates the recirculation when the water parcel is moving outward, favoring a clockwise motion. The effect of the inertial instability is active, but the instability somehow enhances the anticyclonic eddy rather than undermines it. Furthermore, our model results suggest that the stratification confines the development of the inertial instability.

The mechanism of the wake generation is studied by estimating HRS and VBF in the budget of eddy kinetic energy. The comparison between HRS and VBF illustrates that the effect of barotropic instability could not be underestimated and baroclinic instability is not important in the island wake scenario. The VKVS's separation points at both island boundaries have large value of HRS . However, VKVS is not a primary cause of gaining eddy kinetic energy once vortices disengage the boundary, where von Kármán vortices and positive HRS are not synchronized. This indicates that positive HRS is caused by the secondary processes at downstream, i.e., barotropic instability.

The energy that generates island wakes is primarily the current shear in the lateral boundary, which is converted by HRS to the eddy kinetic energy. The value of VBF is substantially small in the wake zone. As a result, barotropic instability could be the major contributor of the eddy kinetic energy, especially at downstream, while baroclinic instability is not critical to be addressed. Chang et al. (2013) suggests that active overturning takes place at the wake's frontal region, which is associated with strong vertical shear. Our model finds that vertical shear is caused by (1) the island-shelf effect and (2) the tilting of the vertical vorticity, inducing the overturning and the corresponding high turbulent kinetic energy (TKE) dissipation rate at the shear layer (frontal region).

A flow passes an obstacle is a classical fluid dynamical problem. However, island wakes in the geophysical system are rather complicated when considering realistic conditions. The wakes induced by Green island (~7 km in diameter) mix the ocean and extract a portion of the Kuroshio energy to form the submesoscale process, i.e., the predominant VKVS along with the secondary processes: the barotropic instability and inertial instability. Our results are applicable to the wakes in the lee of small islands standing at a strong current,

especially the western boundary current. Our model results suggest that the hot spot of turbulence mixing is the zone of free shear layer, which is critical for studying the impact of the wake-induced turbulence mixing on the Kuroshio water. Further observational evidence is needed. Our numerical simulation suggests the wake period is ~ 12 h, close to that from observations. The wake period inferred from the *Re-St* relationship lend further support. However, the period is close to semidiurnal tide period. Since the tides are ubiquitous in the ocean, it is important to further clarify the role of tidal current on the wake evolution. Further studies with simulation incorporating tide and in situ moored measurements of the wake are needed to improve the applicability of our results.

Acknowledgments

The authors thank the crew and officers of the R/V *Ocean Researcher III* for their contribution to the ship operation and the field experiments. Thanks also to Wei-Ting Hung, Bee Wang, Wan-Ting Hsieh, Sin Huei Yu, Chieh-Yuan Tsai, and Sin-Ya Jheng for helping us accomplish the shipboard observations. Discussions with Dr. Shih-Nan Chen, Dr. Yu-heng Tseng, Dr. Sen Jan, and Dr. Yu-Hsin Cheng significantly improved our numerical simulations. The authors would like to thank an anonymous reviewer for the constructive comments and for the time taken to help us improve the preliminary manuscript. Chih-Lun Liu was supported by the Ministry of Science and Technology (MOST) under grant 105–2611-M-002–012 and Ming-Huei Chang was supported by MOST under grants 105–2119-M-002–042 and 105–2611-M-002–012. We thank the MOST Ocean Data Bank for providing the historical bathymetry data (<http://www.odb.ntu.edu.tw/odben/>). The data of the field observations and the model output can be obtained at <http://doi.org/10.5281/zenodo.1243319>. The code of the numerical model used in this work is available from <http://mitgcm.org/>.

References

- Adcroft, A., Campin, J., Dutkiewicz, M., Evangelinos, S., Ferreira, C., Forget, D., et al. (2011). *MITgcm user manual* (79 p). MIT/EAPS. Retrieved from http://mitgcm.org/r2_manual/latest/online_documents/manual.html
- Apel, J. R. (1987). *Principles of ocean physics* (631 p.). San Diego, CA: Academic Press.
- Baines, P. G., & Davies, P. A. (1980). Laboratory studies of topographic effects in rotating and/or stratified fluids. In *Orographic effects in planetary flows* (GARP Publ. Ser. 23, pp. 233–299). Geneva, Switzerland: World Meteorological Organization.
- Caldeira, R. M. A., Marchesiello, P., Nezlin, N. P., DiGiacomo, P. M., & McWilliams, J. C. (2005). Island wakes in the Southern California Bight. *Journal of Geophysical Research*, *110*, C11012. <https://doi.org/10.1029/2004JC002675>
- Caldeira, R. M. A., & Sangrà, P. (2012). Complex geophysical wake flows. *Ocean Dynamics*, *62*(5), 683700.
- Chang, M.-H., Jan, S., Mensah, V., Andres, M., Rainville, L., Yang, Y. J., et al. (2018). Zonal migration and transport variations of the Kuroshio east of Taiwan induced by eddy impingements. *Deep-Sea Research Part I*, *131*, 1–15.
- Chang, M.-H., Jheng, S. Y., & Lien, R.-C. (2016). Trains of large Kelvin-Helmholtz billows observed in the Kuroshio above a seamount. *Geophysical Research Letters*, *43*, 8654–8661. <https://doi.org/10.1002/2016GL069462>
- Chang, M. H., Tang, T. Y., Ho, C. R., & Chao, S. Y. (2013). Kuroshio-induced wake in the lee of Green Island off Taiwan. *Journal of Geophysical Research: Oceans*, *118*, 1508–1519. <https://doi.org/10.1002/jgrc.20151>
- Chavanne, C., Flament, P., & Gurgel, K.-W. (2010). Interactions between a submesoscale anticyclonic vortex and a front. *Journal of Physical Oceanography*, *40*(8), 1802–1818.
- Coelho, P. M., & Pinho, F. T. (2003). Vortex shedding in cylinder flow of shear-thinning fluids II. Flow characteristics. *Journal of Non-Newtonian Fluid Mechanics*, *110*, 177–193.
- Coutis, P. F., & Middleton, J. H. (2002). The physical and biological impact of a small island wake in the deep ocean. *Deep-Sea Research Part I*, *49*, 1341–1361. [https://doi.org/10.1016/S0967-0637\(02\)00029-8](https://doi.org/10.1016/S0967-0637(02)00029-8)
- Cushman-Roisin, B., & Beckers, J.-M. (2009). *Introduction to geophysical fluid dynamics*. San Diego, CA: Academic Press.
- Dong, C., McWilliams, J. C., & Shchepetkin, A. F. (2007). Island wakes in deep water. *Journal of Physical Oceanography*, *37*(4), 962–981. <https://doi.org/10.1175/JPO3047.1>
- Doty, M. S., & Oguri, M. (1956). The island mass effect. *ICES Journal of Marine Science*, *22*(1), 33–37. <https://doi.org/10.1093/icesjms/22.1.33>
- Gerdes, R., Cornelia, K., & Jürgen, W. (1991). The influence of numerical advection schemes on the results of ocean general circulation models. *Climate Dynamics*, *5*(4), 211–226. <https://doi.org/10.1007/BF00210006>
- Gula, J., Molemaker, M. J., & McWilliams, J. C. (2015). Topographic vorticity generation, submesoscale instability and vortex street formation in the Gulf Stream. *Geophysical Research Letters*, *42*, 4054–4062. <https://doi.org/10.1002/2015GL063731>
- Hasegawa, D., Yamazaki, H., Lueck, R. G., & Seuront, L. (2004). How islands stir and fertilize the upper ocean. *Geophysical Research Letters*, *31*, L16303. <https://doi.org/10.1029/2004GL020143>
- Holton, J. R. (1992). *An introduction to dynamic meteorology* (3rd ed., 511 p.). San Diego, CA: Academic Press.
- Huang, S. J., Ho, C. R., Lin, S. L., & Liang, S. J. (2014). Spatial-temporal scales of Green Island wake due to passing of the Kuroshio current. *Journal International Journal of Remote Sensing*, *35*, 4484–4495. <https://doi.org/10.1080/01431161.2014.916047>
- Hsu, P. C., Chang, M. H., Lin, C. C., Huang, S. J., & Ho, C. R. (2017). Investigation of the island-induced ocean vortex train of the Kuroshio Current using satellite imagery. *Remote Sensing of Environment*, *193*, 54–64. <https://doi.org/10.1016/j.rse.2017.02.025>
- Kang, D., & Curchitser, E. N. (2015). Energetics of eddy-mean flow interactions in the Gulf Stream region. *Journal of Physical Oceanography*, *45*, 1103–1120.
- Kundu, P. K., Cohen, I. M., & Hu, H. H. (2012). *Fluid mechanics* (390 pp.). Amsterdam: Elsevier Academic Press.
- Marshall, J., Adcroft, A., Hill, C., Perelman, L., & Heisey, C. (1997). A finite-volume, incompressible Navier Stokes model for studies of the ocean on parallel computers. *Journal of Geophysical Research*, *102*(C3), 5753–5766. <https://doi.org/10.1029/96JC02775>
- Nunalee, C. G., & Basu, S. (2014). On the periodicity of atmospheric von Kármán vortex streets. *Environmental Fluid Mechanics*, *14*(6), 1335–1355. <https://doi.org/10.1007/s10652-014-9340-9>
- Relf, E. F., & Simmons, L. F. G. (1924). LIII. On the frequency of the eddies generated by the motion of circular cylinders through a fluid. *Philosophical Magazine and Journal of Science*, *49*(290), 509–511. <https://doi.org/10.1080/14786442508634628>
- Roshko, A. (1993). Perspectives on bluff body aerodynamics. *Journal of Wind Engineering*, *49*, 79–100.
- Thomas, L. N., Tandon, A., & Mahadevan, A. (2008). Submesoscale processes and dynamics. In Hecht, M. W. & Hasumi, H. (Eds.), *Ocean modeling in an eddying regime* (pp. 17–38). Washington, DC: American Geophysical Union. <https://doi.org/10.1029/177GM04>
- Tomczak, M. (1988). Island wakes in deep and shallow water. *Journal of Geophysical Research*, *93*(C5), 5153. <https://doi.org/10.1029/JC093iC05p05153>
- Tritton, D. J. (1988). *Physical fluid dynamics* (22 p.). Oxford, UK: Oxford Science Publishers.
- Tseng, Y.-H. (2008). High-order essentially local extremum diminishing schemes for environmental flow. *International Journal for Numerical Methods in Fluids*, *58*, 213–235. <https://doi.org/10.1002/flid.1725>
- von Kármán, T., & Rubach, H. (1912). Über den mechanismus des flüssigkeits—und luftwiderstandes. *Zeitschrift für Physik*, *13*, 49–59.
- Williamson, C. H. K. (1996). Vortex dynamics in the cylinder wake. *Annual Review of Fluid Mechanics*, *28*, 477–539.
- Williamson, C. H. K., & Brown, G. L. (1998). A series in $1/\sqrt{\text{Re}}$ to represent the Strouhal-Reynolds Number relationship of the cylinder wake. *Journal of Fluids and Structures*, *12*, 1073–1085. <https://doi.org/10.1006/jfls.1998.0184>
- Wolanski, E., & Hamner, W. M. (1988). Topographically controlled fronts in the ocean and their biological influence. *Science*, *241*(4862), 177–181. <https://doi.org/10.1126/science.241.4862.177>